RSC Advances

PAPER

View Article Online
View Journal | View Issue

Cite this: *RSC Adv.*, 2020, **10**, 22183

Synergistic effect of trivalent (Gd^{3+}, Sm^{3+}) and high-valent (Ti^{4+}) co-doping on antiferromagnetic $YFeO_3$

P. S. J. Bharadwaj, [a] Swarup Kundu, [a] Vijay Sai Kollipara *[a] and Kalidindi B. R. Varma [ab]

Monophasic polycrystalline powders of $Y_{1-x}R_xFe_{1-(4/3)y}Ti_yO_3$ (R = Sm, Gd; x = 0.05, 0.10, 0.15; y = 0.05) were successfully synthesized *via* a low temperature solid-state synthesis route. The X-ray diffraction and Raman spectroscopy studies indicate that all the calcined powders with R^{3+} (Gd^{3+}, Sm^{3+}) at Y^{3+} and Ti^{4+} at Fe^{3+} sites were crystallized in an orthorhombic phase associated with a change in lattice parameters. The Williamson–Hall method employed to calculate the strain revealed that the strain increased with the increased concentration of dopants ((Gd^{3+}, Sm^{3+}) at Y^{3+}) compared to an increase in the size of crystallites, corroborating the findings of SEM. Analysis of diffuse reflectance spectra indicated a drop in bandgap from 1.93 eV to 1.86 eV and 1.96 eV to 1.91 eV for Gd, Ti co-doping and Sm, Ti co-doping respectively, demonstrating the capacity of the synthesized powders to absorb visible light. Absorbance spectra also revealed the existence of mixed states of Fe^{3+} and Fe^{4+} which was corroborated by XPS studies. The magnetic hysteresis loop analysis at room temperature illustrated that with co-doping, there is a strong enhancement in magnetization as well as coercivity, suggesting a strong transition from antiferromagnetic behaviour to ferromagnetic behaviour. Pertaining to the greatly improved optical and magnetic properties with the addition of (Gd^{3+}, Sm^{3+}) at Y^{3+} and Ti^{4+} at Fe^{3+} sites, these materials are anticipated to be of potential use in various applications.

Received 19th March 2020
Accepted 2nd June 2020

DOI: 10.1039/d0ra02532a

rsc.li/rsc-advances

Introduction

The existence of various physical properties associated with a single phase material has resulted in the study of and technological interest in multiferroic materials.[1] These multiferroic materials could be employed for several applications that include temperature induced spin switching,[2] magnetic field induced spin switching,[3,4] solid oxide fuel cells, photo-catalysis, magneto-optical devices, capacitors, magneto-electric sensors in transducers, microwave electronics, and spintronics, owing to their magnetic and electric polarization effects.[5–7] $RFeO_3$ has a distorted perovskite structure that crystallizes in the orthorhombic *Pmna* space group.[8] The crystallographic unit cell contains 4 equivalent iron (Fe) ions. Although $RFeO_3$ has a distorted structure, FeO_6 remains essentially an octahedron with six oxygen anions surrounding the Fe-ion, leading to crystal field splitting. The typical rare-earth orthoferrite $YFeO_3$ falls into this category. There have been several reports on the dielectric and magnetic properties of $YFeO_3$, even though it did not exhibit conventional ferroelectric effects at room temperature due to its low Curie temperature (−256 °C). Nevertheless, the narrow energy bandgap (1.8–2.6 eV) makes $YFeO_3$ a viable material for magneto-optical applications.[9] The weak ferromagnetic behaviour of $YFeO_3$ is due to the canting of Fe^{3+} ions in an orthorhombic structure. However, it was demonstrated that the magnetic properties of $YFeO_3$ can be enhanced by means of doping. For instance, the non-magnetic Y^{3+} is doped by divalent[10] and trivalent ions[11,12] and Fe^{3+} by trivalent[13] and high valency ions.[14] Doping at Y^{3+} resulted in the improvement of magnetization while the Fe^{3+} doping enhanced the coercivity. To the best of our knowledge, there exist no reports in the literature on co-doping of rare-earth (Gd^{3+}, Sm^{3+}) at Y^{3+} and Ti^{4+} at Fe^{3+}. Therefore the objective of the current report is to investigate into the effect of co-doping of rare-earth (Gd^{3+}, Sm^{3+}) and Ti^{4+} on the structural, magnetic and optical properties of $YFeO_3$.

There are several synthesis routes that are known[15–19] to obtain the polycrystalline powders of $Y_{1-x}R_xFe_{1-(4/3)y}Ti_yO_3$ where R = Gd, Sm. These multiple synthesis routes include the most popular solid-state and sol–gel routes. However, there are certain disadvantages associated with the solid-state synthesis route. First being the formation of secondary phases such as Y_2O_3 and $Y_3Fe_5O_{12}$. Secondly, the existence of a hexagonal phase at low temperatures, which at higher temperatures becomes an orthorhombic phase. Our previous research identified the effective preparation of polycrystalline $YFeO_3$ by sol–gel synthesis route in detail.[12] Sol–gel approach is beneficial relative to the solid-state system because it allows for

[a]*Department of Physics, Sri Sathya Sai Institute of Higher Learning, Prasanthi Nilayam, Andhra Pradesh, India. E-mail: kvijaysai@sssihl.edu.in*
[b]*Materials Research Centre, Indian Institute of Science, Bengaluru, India*

homogeneous mixing of the precursor ions at a molecular level. However, other drawbacks associated with this process are (i) the creation of pores due to the generation and trapping of gases, (ii) the coexistence of hexagonal and orthorhombic phases which could be solved by precisely regulating the calcination temperatures and (iii) usage of certain toxic complexing agents.

In view of the aforementioned disadvantages, an easy and efficient method that is slightly different from the above method has been developed. It is a low temperature solid-state route for the synthesis of $Y_{1-x}R_xFe_{1-(4/3)y}Ti_yO_3$ which has the advantage over other methods in phase purity, precision in phase control, low-cost and ultrafine particle size. This synthetic method was effectively employed to obtain pristine $YFeO_3$.[13]

Materials and methods

The polycrystalline powders of $Y_{1-x}R_xFe_{1-(4/3)y}Ti_yO_3$ (R = Sm, Gd; x = 0.05, 0.10, 0.15; y = 0.05) have been successfully obtained using low temperature solid-state synthesis method. The precursors used were $Y(NO_3)_3\cdot 6H_2O$ (AR grade, purity > 98%), $Fe(NO_3)_3\cdot 9H_2O$ (AR grade, purity > 98%), $Sm(NO_3)_3\cdot 6H_2O$ (Sigma-Aldrich, purity > 99%), $Gd(NO_3)_3\cdot 6H_2O$ (Sigma-Aldrich, purity > 99%), TiO_2 (Sigma-Aldrich, purity > 99%) and citric acid (AR grade, purity > 99%). Initially, the relevant precursors were weighed according to the stoichiometric ratios and were ground in an agate mortar for 30 min. This initial grinding resulted in the formation of light brown mush implicating the complex formation. This mush was then heated at 120 °C for 2 h which facilitated the removal of free water and yielded dark brown powder. These powders were then heated at 350 °C for 6 h to aid the complete decomposition of nitrates. Subsequently, these were finely ground and subjected to heating at 900 °C for 1 h resulting in the formation of monophasic polycrystalline powders. The schematic is given in Fig. 1.

Mechanism of low temperature solid-state synthesis

Solid-state reaction involves four stages (i) diffusion, (ii) reaction, (iii) nucleation and (iv) growth. Diffusion takes place when the reactant or precursor molecules are in contact, followed by chemical reaction yielding the product. The nucleation is completely achieved until the product molecules aggregate to a certain scale. Once the product forms an independent crystal phase, crystal nuclei expand to a certain size. In the low temperature solid-state reaction, the reactants are brought into full contact as they reach a micron-level mixture. This is achieved by grinding the reactants which reduces their size aiding the surface energy to increase. As some of the reactants are hygroscopic, several micron liquid baths are created during the grinding process. This liquid environment helps the surface molecules of the reactants to aggregate and then react rapidly with one another. This results in the reaction to occur faster. The citric acid apart from acting as a chelating or complexing agent, provides the energy in the form of heat during calcination helping $Y_{1-x}R_xFe_{1-(4/3)y}Ti_yO_3$ (R = Sm, Gd; x = 0.05, 0.10, 0.15; y = 0.05) to form at low temperatures.

Characterization

The polycrystalline powders were characterized using X-ray powder diffractometer (X'Pert Pro, Panalytical) with Cu K_α = 1.5408 Å. The average crystallite size and lattice strain of these samples have been determined using Williamson–Hall plots. The structural analysis was further strengthened by recording Raman spectra using Raman microscope, (Thermo Scientific, laser excitation, λ = 780 nm). Microstructural and elemental analyses were performed using Jeol IT300 scanning electron

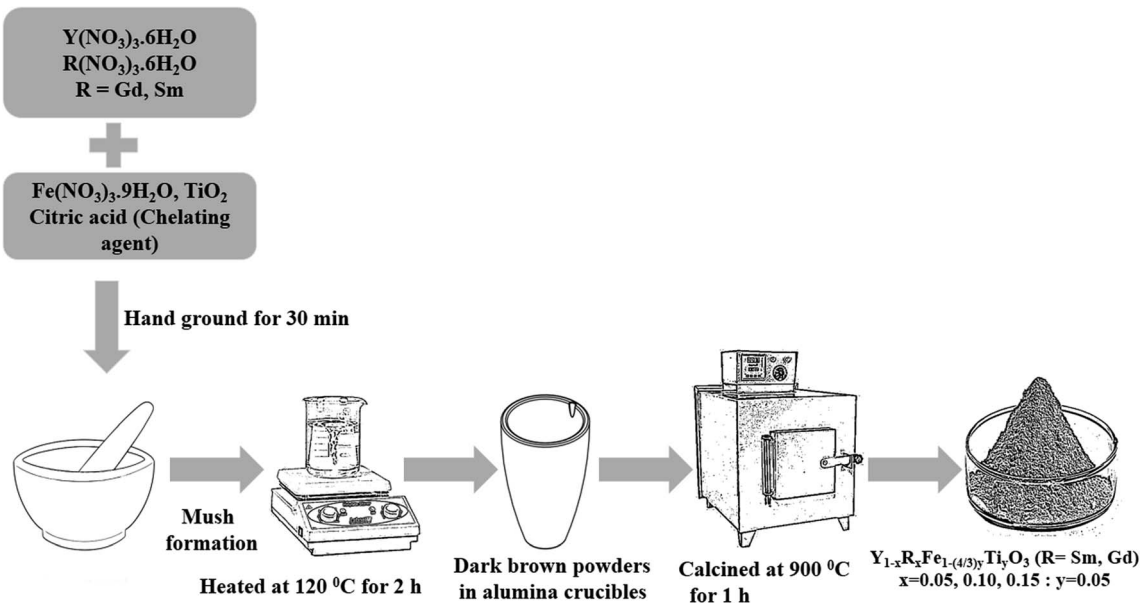

Fig. 1 Schematic of low temperature solid-state synthesis route.

microscope (SEM). Magnetic hysteresis loops at room temperature were obtained using vibrating sample magnetometer (Model EZ9, MicroSense, USA). The bandgap of the polycrystalline powders of the different formulations were measured using diffuse reflectance spectroscopy (DRS) in the range 200–800 nm employing UV-Vis spectrophotometer (Perkin Elmer LS 55). The X-ray photoelectron spectroscopic studies for all the samples were pursued by Fison Instruments S-probe TM2803.

Results and discussion

The room temperature X-ray powder diffraction (XRD) patterns of $Y_{1-x}R_xFe_{1-(4/3)y}Ti_yO_3$ (R = Sm, Gd; x = 0.05, 0.10, 0.15; y = 0.05) are represented in Fig. 2. XRD studies confirmed the formation of monophasic crystalline orthorhombic phase for all the samples under investigation with no detectable impurity peaks. This outcome from XRD studies indicate that the reaction is complete and the products formed are of required purity. The partial substitution of Gd^{3+} (x = 0.05, 0.10, 0.15), Sm^{3+} (x = 0.05, 0.10, 0.15) at Y^{3+} sites and Ti^{4+} (y = 0.05) at Fe^{3+} sites could be evidenced from the downward shift in the peak positions with the increase in dopant concentration, as shown in the insets of Fig. 2. The downward shift in the peak positions with an increase in dopant concentration implies that there is an increase in lattice parameters. For orthorhombic system, the peak positions and lattice parameters are related by $(h/a)^2 + (k/b)^2 + (l/c)^2 = 4\sin^2\theta/\lambda^2$, where h, k, l are Miller indices; a, b, c are lattice parameters; θ is the peak position; λ is the wavelength of the X-rays used. Further, as we are doping Gd^{3+} (x = 0.05, 0.10, 0.15), Sm^{3+} (x = 0.05, 0.10, 0.15) at Y^{3+} sites whose ionic radii (Gd^{3+} = 1.24 Å, Sm^{3+} = 1.10 Å) are relatively higher than that of Y^{3+} (1.06 Å), such shifts are expected. Moreover, if the partial substitution of Gd^{3+}, Sm^{3+} and Ti^{4+} deviates from Y^{3+} and Fe^{3+} respectively, then the secondary phases/impurities must be formed which will reflect as extra peaks in XRD pattern. The absence of detectable X-ray peaks which are unaccounted for in these patterns confirm the effective doping at appropriate sites.

The computed lattice parameters based on XRD data are depicted in Table 1. The values increased with the increase in the rare earth (Gd, Sm) doping concentration at Y^{3+} and decreased with Ti^{4+} doping at Fe^{3+} suggesting the effectiveness of doping of Gd^{3+}, Sm^{3+} which results in the increase in $YFeO_3$ ($r_{Sm^{3+}}$ (1.24 Å) > $r_{Gd^{3+}}$ (1.10 Å) > $r_{Y^{3+}}$ (1.06 Å)) lattice volume, whereas the substitution of Ti^{4+} at Fe^{3+} results in the reduction of $YFeO_3$ ($r_{Fe^{3+}}$ (0.645 Å) > $r_{Ti^{4+}}$ (0.605 Å)) lattice volume.[20] This incessant evolution of lattice parameters also indicate the successful doping of Gd^{3+}, Sm^{3+} of different concentrations at Y^{3+} sites and Ti^{4+} (0.05) at Fe^{3+} sites in $YFeO_3$.

The X-ray diffraction peaks for $Y_{1-x}R_xFe_{1-(4/3)y}Ti_yO_3$ (R = Sm, Gd; x = 0.05, 0.10, 0.15; y = 0.05) powders were indexed to $YFeO_3$ orthorhombic crystal structure (ISCD 98-008-0866) associated with '*Pmna*' space group of '*mmm*' point group. The perovskite (ABO_3) structure incorporating different elements in the periodic table as structural distortion, though ideally it is cubic. These distortions are essentially of three types, tilting of BO_6 octahedra, polar cationic displacement and Jahn–Teller distortions. Out of these three, tilting of BO_6 octahedra is most commonly found in *Pmna* space group to which $YFeO_3$ belongs. The increase in lattice parameters with an increase in dopant concentration leads to an increase in structural distortion. The structural distortion could be calculated using O'Keefe geometric approximation.[21]

$$\theta_1 = \cos^{-1}\left|\frac{2 - 5\cos^2\varphi_1}{2 + \cos^2\varphi_1}\right|$$

$$\theta_2 = \cos^{-1}\left|\frac{1 - 4\cos^2\varphi_2}{3}\right|$$

where θ_1, θ_2 and φ_1, φ_2 are bond angles and octahedral tilt angles respectively.

The sharing of O^{2-} ions between two FeO_6 octahedral structures leads to the formation of two kinds of Fe–O–Fe superexchange bonds, θ_1 and θ_2. These bond angles and tilt angles obtained using crystallographic information data

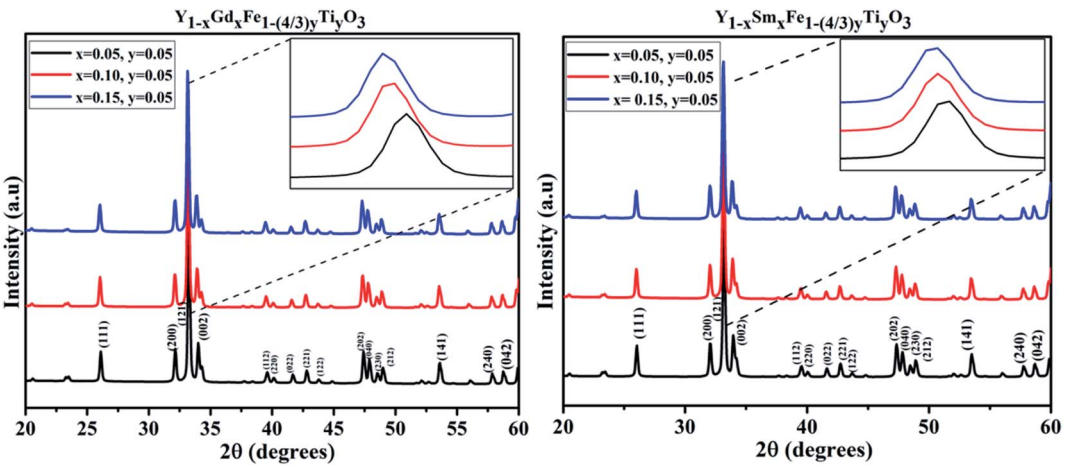

Fig. 2 XRD patterns obtained for $Y_{1-x}R_xFe_{1-(4/3)y}Ti_yO_3$ (R = Sm, Gd; x = 0.05, 0.10, 0.15; y = 0.05).

Table 1 Refinement and lattice parameters of $Y_{1-x}R_xFe_{1-(4/3)y}Ti_yO_3$ (R = Sm, Gd; x = 0.05, 0.10, 0.15; y = 0.05). Characterization tool: XRD

		Lattice parameters			Agreement factors		
Name of the compound	Dopant concentration	a (Å)	b (Å)	c (Å)	R_{wp} (%)	R_p (%)	GOF (%)
YSFTO	$x = 0.05, y = 0.05$	5.589	7.603	5.283	2.73	1.96	1.37
	$x = 0.10, y = 0.05$	5.593	7.619	5.291	3.07	2.24	1.58
	$x = 0.15, y = 0.05$	5.597	7.626	5.307	3.27	2.35	1.61
YGFTO	$x = 0.05, y = 0.05$	5.591	7.613	5.287	3.03	2.15	1.57
	$x = 0.10, y = 0.05$	5.594	7.618	5.294	2.88	2.08	1.64
	$x = 0.15, y = 0.05$	5.601	7.622	5.301	3.26	2.13	1.94

acquired from Reitveld analysis were represented in VESTA software (ver. 3.5.2). The extent of distortion with respect to doping concentration *i.e.*, the change in tilt angles and bond lengths are given in Table 2.

With the doping at Y^{3+} and Fe^{3+} sites the structure should remain as orthorhombic. The phase stability is measured using Goldschmidt tolerance factor which is given by

$$T = \frac{R_A + R_B}{\sqrt{2}(R_B + R_O)}$$

where $R_A^{eff} = R_Y(1 - x) + R_{Sm/Gd}(x)$, $R_B^{eff} = R_{Fe}[1 - (4/3)y] + R_{Ti}(y)$

Crystallite size and strain analysis

The crystallite size could be calculated using Scherrer formula associated with the full width at half maximum of the peaks as given in eqn (1).

$$L = \frac{K\lambda}{\beta \cos\theta} \quad (1)$$

The Bragg peak width of the obtained XRD patterns also consists of instrument broadening effects. To circumvent such aberrations, the diffraction pattern obtained from the standard silicon sample was used to ascertain the instrument broadening. The relation given in eqn (2) is used to obtain the instrument broadening corresponding to the diffraction peaks of the samples under investigation.

Table 2 Bond angles Fe–O–Fe (θ_1, θ_2), bond lengths (Fe–O) and octahedral tilt angles (φ_1, φ_2) of $Y_{1-x}R_xFe_{1-(4/3)y}Ti_yO_3$ (R = Sm, Gd; x = 0.05, 0.10, 0.15; y = 0.05). Characterization tool: XRD

	Bond angles		Tilt angles		Bond length (Å)
Name of the compound	θ_1	θ_2	φ_1	φ_2	(Fe/Ti–O)
$Y_{1-x}Sm_xFe_{1-(4/3)y}Ti_yO_3$					
$x = 0.05, y = 0.05$	144.615	143.59	21.35	22.49	2.032
$x = 0.10, y = 0.05$	144.613	143.582	21.343	22.50	2.035
$x = 0.15, y = 0.05$	144.607	143.570	20.863	22.51	2.037
$Y_{1-x}Gd_xFe_{1-(4/3)y}Ti_yO_3$					
$x = 0.05, y = 0.05$	144.831	143.712	21.22	22.42	2.03
$x = 0.10, y = 0.05$	144.829	143.689	21.21	22.44	2.034
$x = 0.15, y = 0.05$	144.597	143.560	21.42	22.51	2.044

$$\beta_L{}^2 = [\beta_{sample}{}^2 - \beta_{instrumental}{}^2] \quad (2)$$

Further, in doped samples of the present kind, the peak broadening owing to the strain is not completely ruled out. The strain and strain-induced peak broadening are related as given in the following eqn (3).

$$\varepsilon = \frac{\beta_s}{4 \tan\theta} \quad (3)$$

Scherrer equation is reliant on diffraction angle θ as $1/\cos\theta$ but not as $\tan\theta$ as in Williamson–Hall (W–H) method. It implies that Scherrer formula considers only the instrumental broadening but not the strain-induced broadening.

The Williamson–Hall (W–H) equation assumes that the contribution of strain and crystallite size to peak broadening are independent to each other. Therefore the W–H equation is a simple sum of eqn (1) and (3) which is given by

$$\beta_{hkl} = \beta_s + \beta_L \quad (4)$$

$$\beta_{hkl} = \frac{K\lambda}{L \cos\theta} + 4\varepsilon \tan\theta \quad (5)$$

The above equation can be rearranged in the form given below

$$\beta_{hkl}\cos\theta = \frac{K\lambda}{L} + 4\varepsilon \sin\theta \quad (6)$$

We have employed W–H method (eqn (6)) to perform both crystallite size and strain analysis depending on different θ positions. The W–H plots are depicted in Fig. 3 for all $Y_{1-x}R_xFe_{1-(4/3)y}Ti_yO_3$ (R = Sm, Gd; x = 0.05, 0.10, 0.15; y = 0.05) samples that are drawn with 4 sin θ along x-axis and β_{hkl} cos θ along y-axis. The crystallite size was calculated from the y-intercept and the strain was derived from the slope of the linear fit to the data, respectively. The W–H method assumes the strain to be isotropic and identical along all crystallographic directions. The crystallite size and strain for different compositions of $Y_{1-x}R_xFe_{1-(4/3)y}Ti_yO_3$ (R = Sm, Gd; x = 0.05, 0.10, 0.15; y = 0.05) are illustrated in Table 3.

Analysis of crystal structure is considered to be incomplete until it is substantiated by fitting with various crystallographic parameters and multiple pattern variables with a chosen structural

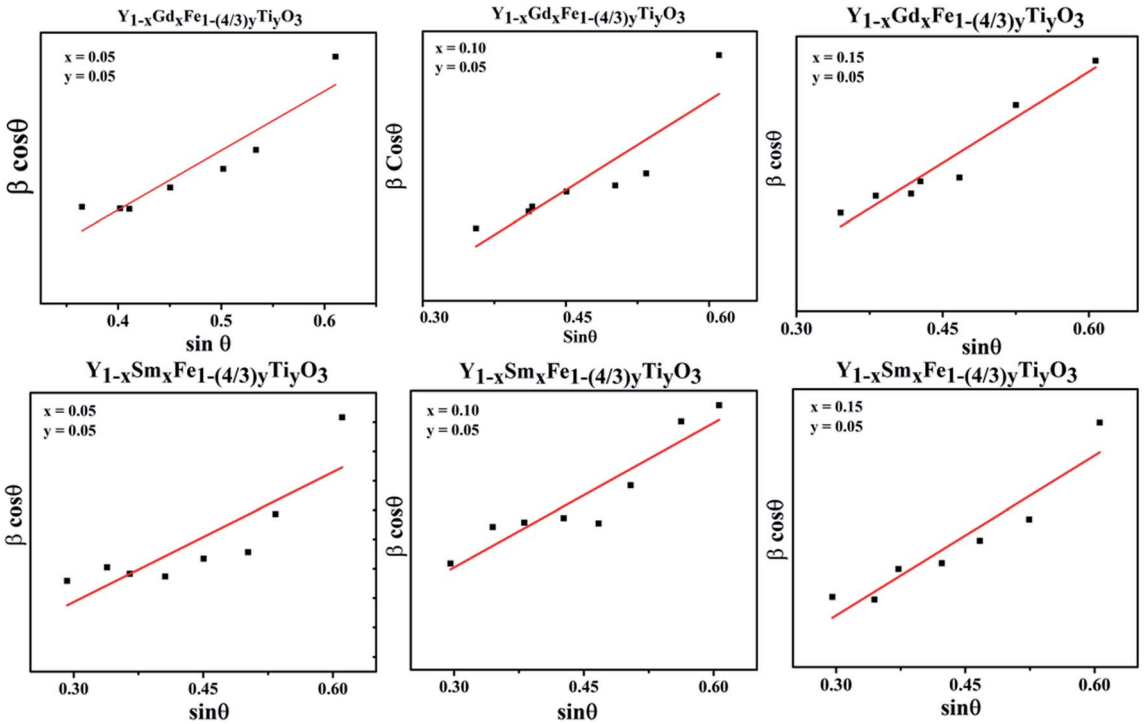

Fig. 3 Williamson–Hall plots for $Y_{1-x}R_xFe_{1-(4/3)y}Ti_yO_3$ (R = Sm, Gd; $x = 0.05, 0.10, 0.15$; $y = 0.05$).

model from database. Rietveld proposed a method wherein the individual intensities at each step of powder diffraction data was fit. In this method, a least square technique was incorporated till the best fit is attained between observed powder diffraction data and calculated pattern from the selected model in the database. Rietveld refinement was incorporated to ascertain the validity of orthorhombic structural model and to precisely calculate the lattice parameters. The Rietveld refined plots are depicted in Fig. 4. The Rietveld refinement was done using High score plus software. The experimental data are depicted as transparent rings, while the calculated intensities are depicted as solid lines. The Bragg positions for '*Pmna*' space group are depicted by the vertical lines at the bottom. The disparity between observed and measured intensities are seen in the form of solid lines in all the figures. The background is corrected using pseudo-voigt function. Parameters like scale factors, shape parameters, isothermal parameters, occupancies and lattice constants were taken to be fixed during the refinement process. We considered oxygen positions to be free parameters whereas other atomic positions were taken to be fixed. The R_{wp}, weighted profile residual factor which accounts for the background, the R_p, profile residual factor that only takes peaks into account without accounting the background and the goodness of fit (GOF) which describes how well it fits into a set of observations, were found to be low, suggesting the goodness of refinement. The refined lattice parameters and agreement factors are given Table 1.

Raman studies

Generally, ABO_3 perovskite has a cubic structure with corner-linked BO_6 octahedra with B cations at the centre and A cations in the space between the octahedral, respectively. Raman scattering is forbidden due to symmetry in cubic perovskite structure. From the XRD studies, it is evidenced that samples with different configurations under study are typical

Table 3 Goldschmidt tolerance factor, crystallite size, lattice strain obtained for $Y_{1-x}R_xFe_{1-(4/3)y}Ti_yO_3$ (R = Sm, Gd; $x = 0.05, 0.10, 0.15$; $y = 0.05$). Characterization tool: XRD

Name of the compound	Dopant concentration	Crystallite size (nm)	Strain	Tolerance factor
YSFTO	$x = 0.05, y = 0.05$	112.3	0.273	0.863
	$x = 0.10, y = 0.05$	119.6	0.284	0.865
	$x = 0.15, y = 0.05$	124.2	0.317	0.868
YGFTO	$x = 0.05, y = 0.05$	104.3	0.254	0.859
	$x = 0.10, y = 0.05$	115.8	0.281	0.861
	$x = 0.15, y = 0.05$	121.7	0.307	0.859

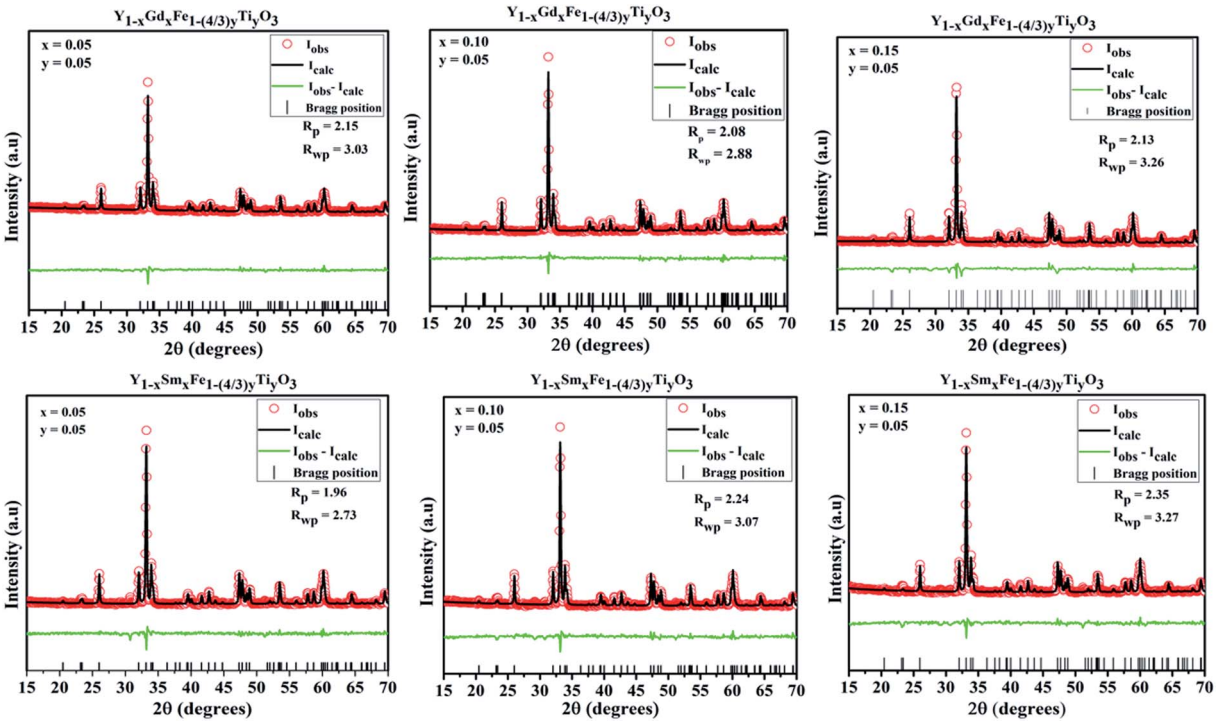

Fig. 4 Rietveld refined plots for $Y_{1-x}R_xFe_{1-(4/3)y}Ti_yO_3$ (R = Sm, Gd; $x = 0.05, 0.10, 0.15$; $y = 0.05$).

example of perovskite structure (ABO_3) and crystallize in orthorhombic structure with *Pmna* space group. The antiphase tilt of FeO_6 octahedra gives rise to the distorted orthorhombic structure. This tilting of FeO_6 octahedra necessarily introduces a distortion in the RO_{12} icosahedron (polyhedron).

As per group theory, the orthorhombic *Pmna* structure has 24 Raman active modes $7A_g + 5B_{1g} + 7B_{2g} + 5B_{3g}$. Out of these modes 12 are first order Raman modes.[22] The Raman spectra for the system $Y_{1-x}R_xFe_{1-(4/3)y}Ti_yO_3$ (R = Sm, Gd; $x = 0.05, 0.10, 0.15$; $y = 0.05$) is presented in the Fig. 5.

The structural analysis could be done by analyzing the Raman bands in the four different spectral regions.

(i) Region 1: 120–200 cm^{-1}, with two peaks 149 cm^{-1} and 177 cm^{-1} which are attributed to the vibrations of yttrium ion. According to harmonic oscillator approximation $\omega \sim (k/M)^{1/2}$, where ω is the frequency, k is the spring constant and M is atomic mass, the heaviest atom is predicted to vibrate in low wavenumber region and this justifies the shift in the peaks with different dopants and different doping concentrations.

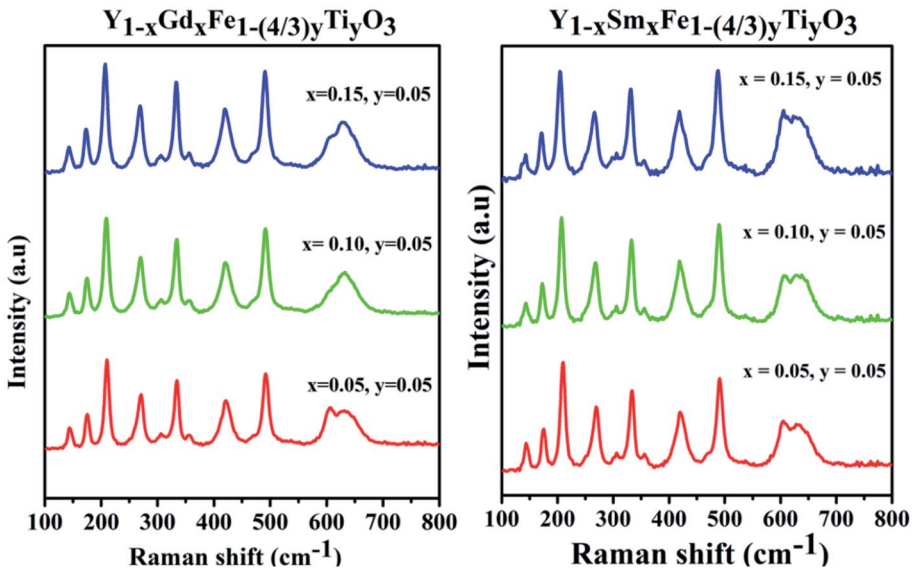

Fig. 5 Raman spectra for $Y_{1-x}R_xFe_{1-(4/3)y}Ti_yO_3$ (R = Sm, Gd; $x = 0.05, 0.10, 0.15$; $y = 0.05$).

(ii) Region 2: 200–380 cm^{-1}, characterized by 3 different bands. The band at 220 cm^{-1} is attributed to Fe^{3+} ion vibration and the bands around 270 cm^{-1} and 340 cm^{-1} are attributed to Fe^{3+} magnetic ions excitation.

(iii) Region 3: 380–550 cm^{-1}, with two bands of different intensities at 430 cm^{-1} and 481 cm^{-1} which are attributed to the excitation of Fe^{3+} magnetic ions.

(iv) Region 4: 550–800 cm^{-1}, characterized by two partially overlapping bands around 600 cm^{-1}, one band is a characteristic of Fe–O bond. The appearance of a second band which is not observed in pristine $YFeO_3$ might be due to the doping of Ti^{4+} at Fe^{3+} sites.

The surface morphology of all the synthesized powdered samples was depicted using backscattered electron micrographs as shown in Fig. 6. All the powder samples were sputtered by platinum to avoid surface charging and were mounted using carbon tape. The samples under study exhibit only one region with uniform colour tonality which is associated with the electron density, proving that all the synthesized samples are monophasic without any impurity phases. The crystallite size distributions are depicted in each micrograph as the insets. The log normal function was used to fit the obtained data.

$$f(D) = \frac{1}{\sqrt{2}\pi\sigma D}\exp\left[-\ln^2(D/D_0)/2\sigma^2\right]$$

where $\langle D\rangle = D_0\exp(\sigma^2/2)$

And the mean particle size is given by

$$\sigma_D = \langle D\rangle[\exp(\sigma^2) - 1]^{1/2}$$

It is observed that the crystallite size increased from 0.28 μm to 0.44 μm for $Y_{1-x}Sm_xFe_{1-(4/3)y}Ti_yO_3$ ($x = 0.05, 0.10, 0.15$; $y = 0.05$) with an error bar of 0.0173 to 0.0241 (Fig. 6a–c) and from 0.49 μm to 0.60 μm for $Y_{1-x}Gd_xFe_{1-(4/3)y}Ti_yO_3$ ($x = 0.05, 0.10, 0.15$; $y = 0.05$) with an error bar of 0.0156 to 0.0210. The reason for such an increase in crystallite size with an increase in dopant concentration could also be due to the reduction of oxygen vacancies. The heterovalent doping of Ti^{4+} at Fe^{3+} results in the charge compensation by impregnating such vacancies. This is evidenced by the reduction of pores which can be observed in Fig. 6. Moreover, the partial replacement of Ti^{4+} whose ionic radii and atomic weight lower than that of Fe^{3+} enhances the grain growth.[22] The crystallite size calculated from XRD analysis varies significantly from that obtained by the SEM analysis. This is ascribed to the agglomeration effects owing to their smaller size and innate magnetism.[23]

The energy dispersive X-ray spectra (EDS) of all the synthesized show the peaks associated with Y, Sm, Gd, Fe, Ti and O atoms. The peaks associated with 2.07 keV and 0.27 keV were attributed to Pt and carbon tape (used for sample preparation) respectively. Apart from proving the existence of all the elements associated with the samples under investigation, the EDS spectrum quantifies their relative proportions reasonably well. The lack of elemental impurities in the synthesized samples could be evidenced by the absence of unaccounted peaks (Table 4).

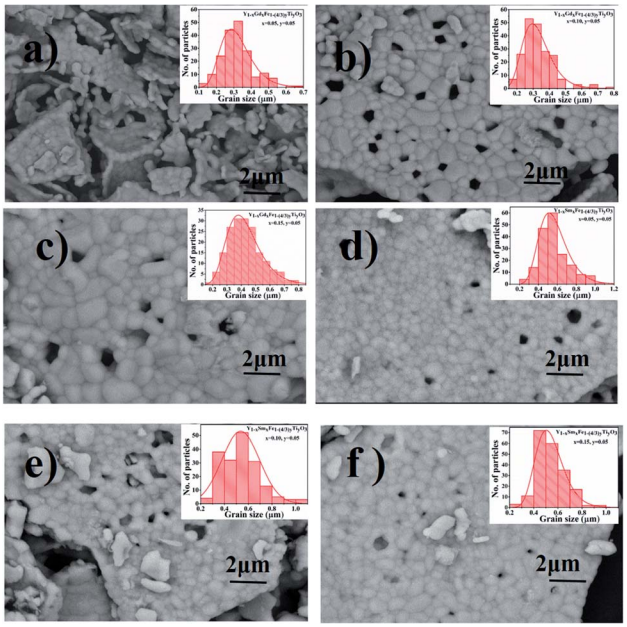

Fig. 6 SEM micrographs of (a) $Y_{1-x}R_xFe_{1-(4/3)y}Ti_yO_3$ ($x = 0.05$, $y = 0.05$), (b) $Y_{1-x}Gd_xFe_{1-(4/3)y}Ti_yO_3$ ($x = 0.10$, $y = 0.05$), (c) $Y_{1-x}Gd_xFe_{1-(4/3)y}Ti_yO_3$ ($x = 0.15$, $y = 0.05$) (d) $Y_{1-x}Sm_xFe_{1-(4/3)y}Ti_yO_3$ ($x = 0.05$, $y = 0.05$), (e) $Y_{1-x}Sm_xFe_{1-(4/3)y}Ti_yO_3$ ($x = 0.10$, $y = 0.05$), (f) $Y_{1-x}Sm_xFe_{1-(4/3)y}Ti_yO_3$ ($x = 0.15$, $y = 0.05$).

Optical properties

The optical properties unravel the changes that take place in the noticeable Fe d–d transitions which appear in the visible region and uncover the changes that are likely to occur in the bandgap of the material. Diffuse reflectance spectroscopy (DRS) was invoked to study the absorption characteristics and variation in the bandgap with a change in doping concentration. Scattered radiation excluding the specular reflected radiation is collected which matches closely with the Kubelka–Munk function which is given by $F(R) = (1 - R)^2/2R$, where R is the diffuse reflectance.[24]

The absorbance *vs.* wavelength plots for all the samples under study are shown in Fig. 7. The Kubelka–Munk function was used to formulate the $[F(R)h\nu]^2$ *vs.* $h\nu$, where h is Planck's constant and ν is the frequency of the source of illumination. The optical band gap energy, E_g, is derived from the intersection of the tangent line at $[F(R)h\nu]^2 = 0$. These plots are shown as the insets in Fig. 7 and the band gap values are given in Table 5.

In the absorbance plots, there is a strong transition in the range 500–600 nm which corresponds to the electronic transitions implying the charge transfer from valence band of oxygen (O) 2p states to conduction band of iron (Fe) 3d states. These are the allowed p–d transitions.[25,26] The octahedral crystal field splitting of BO_6 octahedra in ABO_3 type perovskite gives rise to splitting of d-orbital into the sub-orbitals of t_{2g} (d_{xy}, d_{yz}, d_{xz}) and e_g ($d_{x^2-y^2}$, d_{z^2}). The intensities of the d–d transitions that occur from t_{2g} to e_g orbitals were observed to be 10^3 times lower than the dipole allowed p–d transitions (O 2p–Fe 3d).[27] In the present study, Fe occupies 3+ oxidation state that is to say it is a d^5 system. The d–d transitions in d^5 system are forbidden by

Table 4 Atomic percentage of the different elements present in $Y_{1-x}R_xFe_{1-(4/3)y}Ti_yO_3$ (R = Sm, Gd; $x = 0.05, 0.10, 0.15$; $y = 0.05$). Characterization tool: EDS

		Atomic%					
Name of the Compound	Dopant concentration	Y L	Sm L	Gd L	Fe K	Ti K	O K
YSFTO	$x = 0.05, y = 0.05$	17.45	2.21	—	27.04	2.54	50.76
	$x = 0.10, y = 0.05$	16.81	3.15	—	28.12	2.63	49.29
	$x = 0.15, y = 0.05$	15.92	4.23	—	28.97	2.74	51.86
YGFTO	$x = 0.05, y = 0.05$	17.77	—	2.66	26.7	2.69	50.18
	$x = 0.10, y = 0.05$	16.37	—	3.25	27.4	2.7	50.28
	$x = 0.15, y = 0.05$	15.99	—	4.1	28.5	2.61	48.8

electric dipole selection rule ($\Delta l = \pm 1$) and spin selection rule ($\Delta S = 0$).[27] Even though $RFeO_3$ samples were dominated by exchange interactions of p–d transitions, we observed the d–d transitions for all the samples under investigation. It is evident from the appearance of intense bands around 1.7 eV in the Tauc plots (Fig. 8).

Tanabe–Sugano (T–S) diagrams were reported to be used to determine the energies of Fe^{2+} ($3d^6$), Fe^{3+} ($3d^5$), Fe^{4+} ($3d^6$) systems.[28] T–S diagrams envisage the zero spin allowed d–d transitions for Fe^{3+}, while they project the spin allowed d–d transitions for Fe^{2+} which is from $t_{2g}^4e_g^2$–$t_{2g}^3e_g^3$ at 1.277 eV and Fe^{4+} which is from $t_{2g}^3e_g^1$–$t_{2g}^2e_g^2$ at 1.72 eV.[28] In the present study, the bands around 1.7 eV are attributed to the spin allowed d–d transitions, which comply with the T–S diagrams of spin allowed d–d transitions of Fe^{4+}. It should be noted from these observations in the absorption spectra of $Y_{1-x}R_xFe_{1-(4/3)y}Ti_yO_3$ (R = Sm, Gd; $x = 0.05, 0.10, 0.15$; $y = 0.05$), that Fe essentially exists in the mixed states of Fe^{3+} and Fe^{4+}. This can be further supported by XPS studies. The existence of mixed states of iron can be attributed to the doping effect.

Table 5 Energy bandgap values for $Y_{1-x}R_xFe_{1-(4/3)y}Ti_yO_3$ (R = Sm, Gd; $x = 0.05, 0.10, 0.15$; $y = 0.05$). Characterization tool: UV-Vis

Name of the compound	Dopant concentration	E_g (eV)	Error
YGFTO	$x = 0.05, y = 0.05$	1.96178	0.03021
	$x = 0.10, y = 0.05$	1.95268	0.02892
	$x = 0.15, y = 0.05$	1.913224	0.02756
YSFTO	$x = 0.05, y = 0.05$	1.930412	0.02791
	$x = 0.10, y = 0.05$	1.910113	0.03219
	$x = 0.15, y = 0.05$	1.86448	0.03428

XPS analysis

X-ray photon spectroscopy that provides with a comprehensive estimate of the chemical states of the elements present in the $Y_{1-x}R_xFe_{1-(4/3)y}Ti_yO_3$ (R = Sm, Gd; $x = 0.05, 0.10, 0.15$; $y = 0.05$) was performed. The deconvolution of Fe $2P_{3/2}$ peak has been done using Shirley background and Gaussian–Lorentzian fitting. The deconvolution gives rise to two different peaks with binding energies around 709.64 eV and 710.72 eV

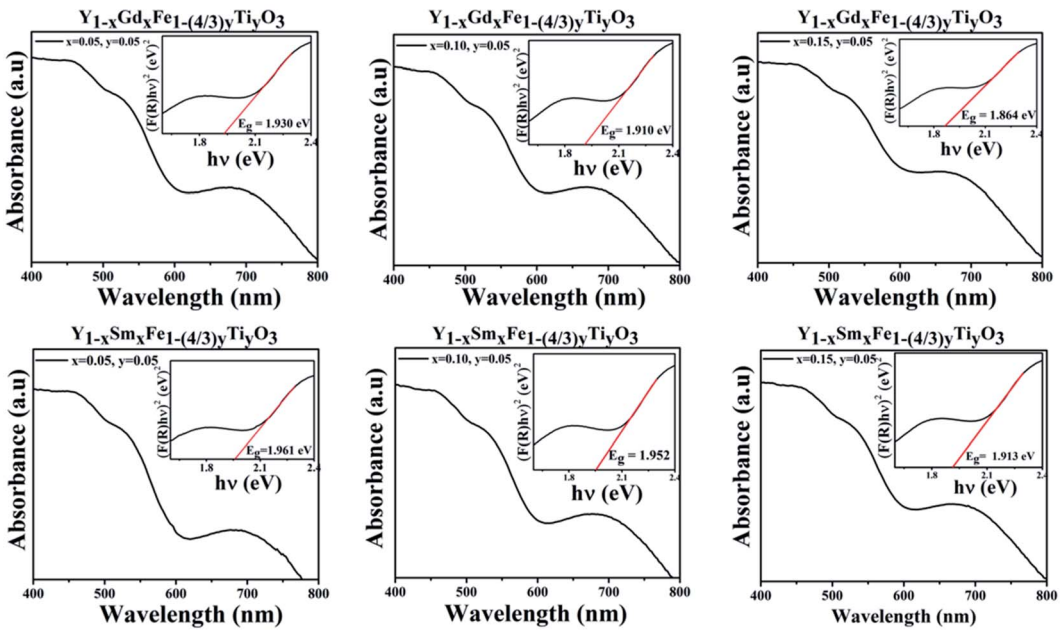

Fig. 7 Absorption spectra and corresponding Tauc plots for $Y_{1-x}R_xFe_{1-(4/3)y}Ti_yO_3$ (R = Sm, Gd; $x = 0.05, 0.10, 0.15$; $y = 0.05$).

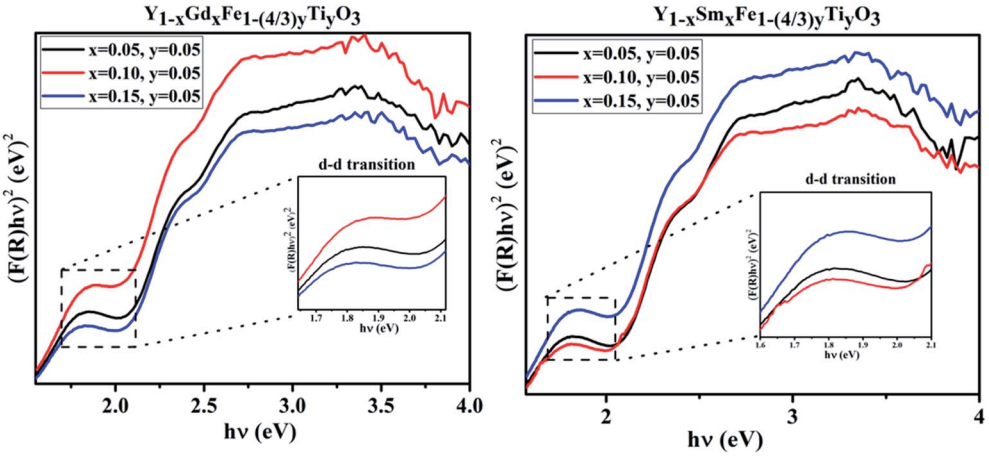

Fig. 8 d–d transitions from the Tauc plots of $Y_{1-x}R_xFe_{1-(4/3)y}Ti_yO_3$ (R = Sm, Gd; $x = 0.05, 0.10, 0.15$; $y = 0.05$).

corresponding to Fe^{3+} and Fe^{4+} respectively.[29] It is observed that Fe^{4+} content increased with an increase in dopant concentration at Y^{3+}. There is a significant shift in Fe $2P_{3/2}$ peaks towards higher binding energies as depicted in Fig. 9, implying a gradual increase of charge at Fe site.[30] This shift is related to the increase of relative amounts of Fe^{4+} ions with an increase in dopant concentration. This proves that the Fe exists in mixed oxidation states of Fe^{3+} and Fe^{4+}. The emergence of Fe^{4+} in the synthesized samples is ascribed to the doping of Ti^{4+} at Fe^{3+}; Sm^{3+} and Gd^{3+} at Y^{3+} sites and presence of oxygen vacancies.

Two peaks are shown for O 1s XPS pattern. The peak around 528 eV is attributed to lattice oxygen and peak at 532 eV is attributed to the surface adsorbed oxygen.[31] In case of Sm^{3+} and Gd^{3+} doping with $x = 0.05$, the peak at 528 eV is not so visible. The reason might be the loss of electron making it O^- from O^{2-} ion and giving rise to prominent 532 eV peak, suggesting the higher concentrations of oxygen vacancies. With the increase in dopant concentration at Y^{3+} the height and area of the peak at 528 eV (lattice oxygen peak) gradually increases and becomes more evident. A detailed quantitative analysis was used to evaluate the content of oxygen deficiencies. The oxygen content was separated into lattice oxygen (O^{2-}) and surface adsorbed oxygen (O^-) using deconvolution. We have calculated the atomic ratio of O^{2-}/O^- which gives an estimate of the

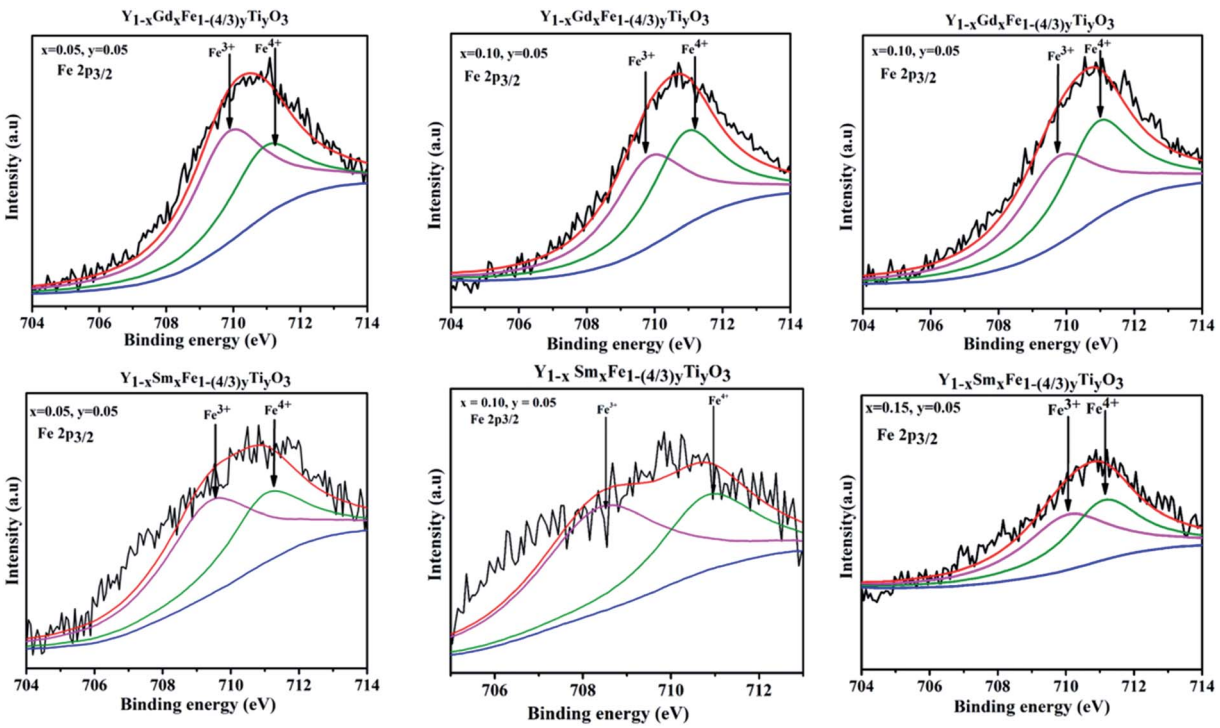

Fig. 9 XPS spectra obtained for Fe $2p_{3/2}$ for $Y_{1-x}R_xFe_{1-(4/3)y}Ti_yO_3$ (R = Sm, Gd; $x = 0.05, 0.10, 0.15$; $y = 0.05$).

concentration of oxygen deficiencies. For $Y_{1-x}Sm_xFe_{1-(4/3)y}Ti_yO_3$ ($x = 0.05, 0.10, 0.15$; $y = 0.05$) the atomic ratio of O^{2-}/O^- increased from 2.19 to 10.134 whereas for $Y_{1-x}Gd_xFe_{1-(4/3)y}Ti_yO_3$ ($x = 0.05, 0.10, 0.15$; $y = 0.05$) O^{2-}/O^- ratio increased from 2.52 to 10.70. This increase in atomic ratio of O^{2-}/O^- with an increase in dopant concentration implies the reduction of concentration of oxygen deficiencies (Fig. 10).

Magnetic properties

The magnetic properties in rare-earth orthoferrites originate from the super-exchange interaction of Fe^{3+}–Fe^{3+}, R^{3+}–R^{3+}, R^{3+}–O^{2-}–Fe^{3+}.[32] The room temperature magnetization *versus* applied magnetic field (M–H) loop of $YFeO_3$ suggests that it is an antiferromagnetic material.[12] The GKA (Goodenough, Kanamori and Anderson) rules predict the antiferromagnetic behaviour of $YFeO_3$ through oxygen mediated super-exchange interaction of pristine $YFeO_3$.[33] As mentioned earlier, the d^5 orbitals of Fe^{3+} split into triply degenerate t_{2g} (d_{xy}, d_{yz}, d_{xz}) and doubly degenerate e_g ($d_{x^2-y^2}$, d_{z^2}) orbitals. The e_g orbitals of Fe^{3+} which are along the crystal axes overlap with 2p orbitals of O^{2-} which give rise to the super-exchange of Fe^{3+}–O^{2-}–Fe^{3+} at 180°. However, the magnetic moment alignment of Fe^{3+} ions is not precisely antiparallel giving rise to the canting of the spins. This results in a small magnetization effect and weak ferromagnetism in $YFeO_3$. Literature reports show that there is an obvious effect on magnetic properties with magnetic and diamagnetic partial substitution/doping.[11,12,34] Fig. 11 gives the M–H hysteresis loops for different compositions of $Y_{1-x}R_xFe_{1-(4/3)y}Ti_yO_3$ (R = Sm, Gd; $x = 0.05, 0.10, 0.15$; $y = 0.05$) at room temperature. There is an increase in magnetization with an increase in dopant concentration at Y^{3+}. However, even at the highest applied magnetic field of 2 T, the magnetization doesn't seem to saturate. The pinching or linear behaviour of pristine $YFeO_3$ is a typical anti-ferromagnetic behaviour. The hysteresis behaviour is attributed to the significantly improved canting of spins. The enhancement in magnetization is due to larger spin canting associated with the presence of Ti^{4+} dopant ions and Fe^{3+} vacancies that are required for restoration of charge balance in the lattice. Also, the uncompensated surface spins of Fe^{3+} ions can enhance the magnetization. Yet another reason might be the formation of Y^{3+}–O^{2-}–R^{3+} instead of R^{3+}–O^{2-}–R^{3+} chain due to large magnetic moment of the dopant ions Gd^{3+}, Sm^{3+}. It is also observed that there a significant enhancement in coercivity. The possible reasons for this might be the formation of frustrated spin systems arising as a result of non-collinear magnetic ordering originating from the presence of uncompensated spins due to partial substitution of Ti^{4+} dopant ions at Fe^{3+} sites and balancing of Fe^{3+} vacancies.

Lattice defects could be introduced by the doping of different radii ions at Y^{3+} site. Host lattice defects that are intrinsic can also be activated when different ions partially occupy Y^{3+} or Fe^{3+} sites which is evident from the increase in lattice constants. The increase in lattice constants with the increase in dopant concentration results in the increase in exchange interaction leading to the enhancement in magnetization. In the scenario of Ti^{4+} doping at Fe^{3+}, the ionic radius of Ti^{4+} is almost similar to that of Fe^{3+}, a strong surface anisotropy plays the major role in the significant increase of coercive field. The enhancement in H_c (coercivity) also suggests the possible existence of ferromagnetic (FM) exchange interaction.

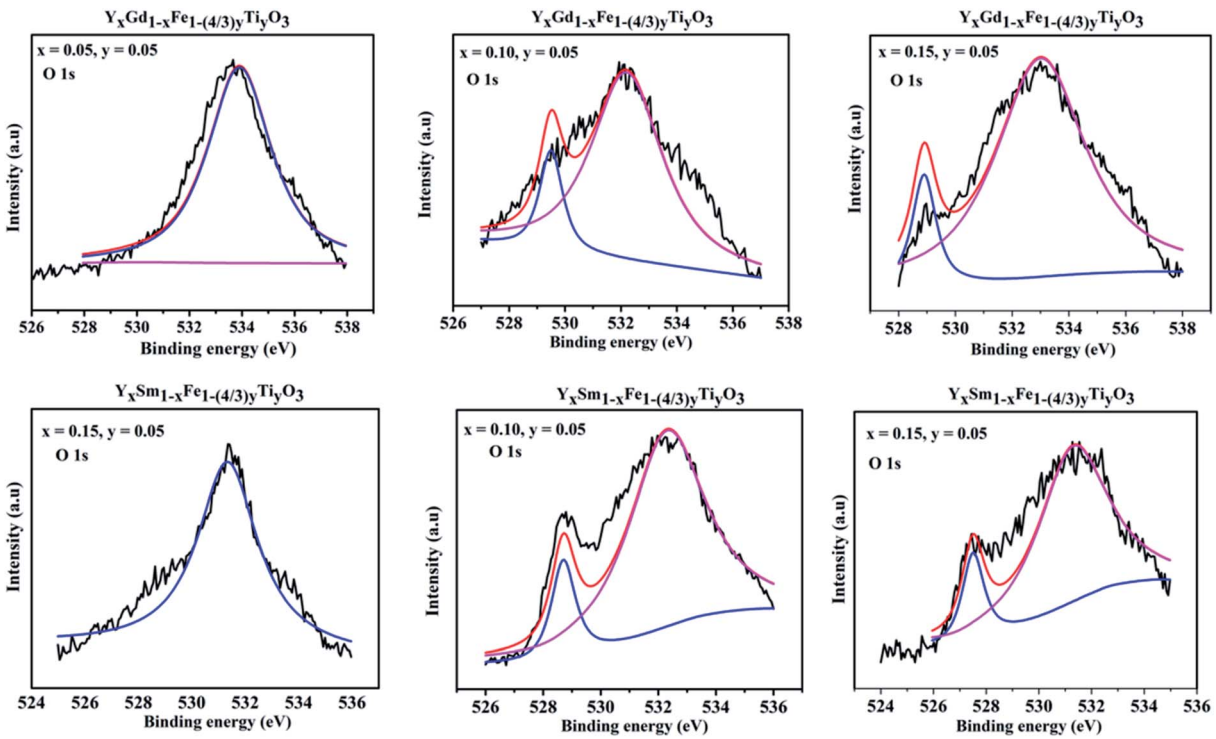

Fig. 10 XPS spectra obtained for O 1s for $Y_{1-x}R_xFe_{1-(4/3)y}Ti_yO_3$ (R = Sm, Gd; $x = 0.05, 0.10, 0.15$; $y = 0.05$).

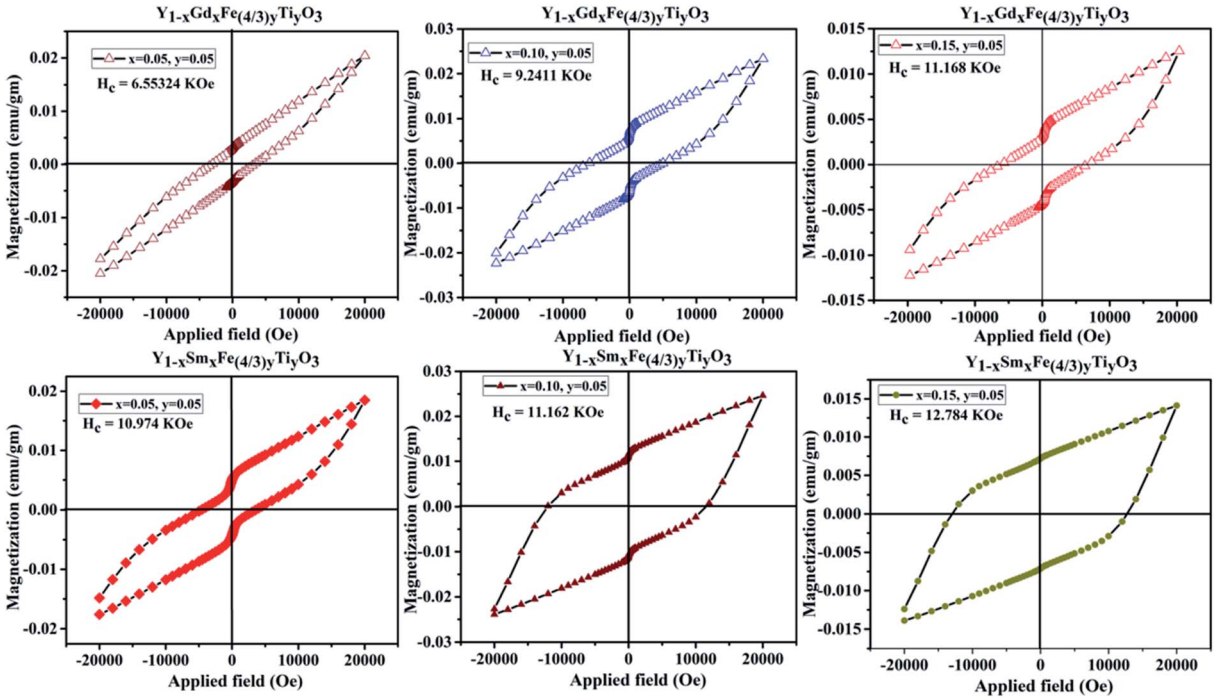

Fig. 11 M-H loops for $Y_{1-x}R_xFe_{1-(4/3)y}Ti_yO_3$ (R = Sm, Gd; $x = 0.05, 0.10, 0.15$; $y = 0.05$).

It should be noted here that Fe–O–Fe super-exchange coupling is a predominant factor in the determination of magnetic ordering. This super-exchange interaction could be influenced by valence states of magnetic ions. Hence, it becomes necessary to have information about valence states of Fe to understand the origin of magnetic behaviour comprehensively. XPS analysis revealed that Fe exists in Fe^{3+} and Fe^{4+} mixed states. The XPS studies revealed that the relative amount Fe^{4+} increases with an increase in dopant concentration. It can also be speculated that the amount of Fe^{4+} increases with a decrease in oxygen deficiencies. This view is supported by our analysis of O 1s XPS pattern in the earlier section. Previous studies have shown that the 180° super-exchange coupling of Fe^{4+}–O^{2-}–Fe^{4+} is ferromagnetic.[35] Therefore, the enhancement in ferromagnetic ordering can be due to Fe^{4+}–O^{2-}–Fe^{4+} super-exchange coupling. However, the presence of Fe^{3+} ions and oxygen deficiencies can induce a different kind of magnetic order which contributes to a small magnetization.[36] It is well known that even a minute structural change/distortion such as tilting of FeO_6 octahedra impact magnetic properties largely. In particular, parameters such as bond angle and bond length which determine orbital overlap, charge transfer and exchange interaction will have a potential effect on magnetic properties. The XPS and VSM analyses carried out on the samples under investigation prompted us to propose two types of exchange coupling interactions *i.e.*, antiferromagnetic super-exchange coupling from Fe^{3+}–O^{2-}–Fe^{3+} and Fe^{4+}–O^{2-}–Fe^{4+} and double exchange coupling from Fe^{3+}–O^{2-}–Fe^{4+}. Also the magnetic properties are affected by oxygen vacancies which interrupt the bridges between O and Fe/Ti and are undesirable from the point of hopping. The detailed quantitative information on the crystallographic changes obtained by XRD and oxygen vacancies allows us to comprehend the magnetic properties correlated by exchange coupling mechanism. We have observed an increase in Fe/Ti–O distance with an increase in dopant (Sm/Gd) concentration, resulting in a decrease in O 2p bandwidth. This decreases the orbital overlap between Fe (3d) and O (2p).

In Fe^{3+}–O^{2-}–Fe^{3+} super-exchange coupling interaction, the charge transfer mainly depends on overlap between Fe (3d) and O (2p) and is maximum when the distortion angle is zero. Such kind of super-exchange leads to anti-ferromagnetism. Since all the prepared samples are in orthorhombic symmetry which is evidenced from Goldschmidt tolerance factor, have the largest deviation from the ideal cubic structure. As the distortion increases with an increase in dopant (Sm^{3+}/Gd^{3+}) concentration listed in the Table 2, the behavior of the samples deviates from antiferromagnetic to ferromagnetic.

In Fe^{3+}–O^{2-}–Fe^{4+}, the conducting electrons hop from Fe^{3+} towards Fe^{4+} *via* O^{2-} bridge is a double exchange coupling interaction. As mentioned earlier, the increase in dopant (Sm^{3+}/Gd^{3+}) concentration at Y^{3+} sites resulted in the increase in Fe/Ti–O distance which consequently reduces the mobility of double exchange electrons which decrease the ferromagnetic property of the prepared samples. However, the reduction in oxygen vacancies evidenced from XPS studies paves the way for the exchange coupling mechanism to take place effectively thus resulting in the improved ferromagnetic behavior of the prepared samples. At this juncture, it is worth mentioning that we did not consider Ti^{4+}–O^{2-}–Ti^{4+} exchange interaction since Ti^{4+} as such is non-magnetic, the doping is comparatively minute and the probability of Ti atoms next to each other is negligibly small considering the random distribution of ions in

Table 6 The maximum magnetization (M_m), remanent magnetization (M_r) and coercivity (H_c). Characterization tool: VSM

Name of the compound	Dopant concentration	M_m (10^{-3}) emu g^{-1}	M_r (10^{-3}) emu g^{-1}	H_c (coercive field) kOe
YSFTO	$x = 0.05, y = 0.05$	14.02	4.62	10.973
	$x = 0.10, y = 0.05$	18.06	7.15	11.162
	$x = 0.15, y = 0.05$	24.27	11.14	12.784
YGFTO	$x = 0.05, y = 0.05$	12.39	3.76	6.551
	$x = 0.10, y = 0.05$	20.47	4.28	9.24
	$x = 0.15, y = 0.05$	22.84	6.26	11.168

$Y_{1-x}R_xFe_{1-(4/3)y}Ti_yO_3$ (R = Sm, Gd; $x = 0.05, 0.10, 0.15$; $y = 0.05$). Table 6 elucidates the maximum magnetization (M_m), remanent magnetization (M_r) and coercivity (H_c) of $Y_{1-x}R_xFe_{1-(4/3)y}Ti_yO_3$ (R = Sm, Gd; $x = 0.05, 0.10, 0.15$; $y = 0.05$).

Conclusions

Phase-pure $Y_{1-x}R_xFe_{1-(4/3)y}Ti_yO_3$ (R = Sm, Gd; $x = 0.05, 0.10, 0.15$; $y = 0.05$) were synthesized *via* low-temperature solid-state synthesis route. Thus prepared powders were found to be orthorhombic matching to that of parent compound $YFeO_3$. The optical bandgap for all the samples under investigation was observed to decrease with the increase in dopant concentration. The enhancement in magnetization and coercivity suggests a transition from antiferromagnetic to ferromagnetic behaviour. The improved magnetic properties are attributed to the existence of Fe^{4+} along with Fe^{3+} and the reduction of oxygen deficiencies.

Funding

This research work did not obtain any particular grants from state, private or non-profit funding agencies.

Conflicts of interest

There are no conflicts to declare.

Acknowledgements

The authors devote the research to the founder chancellor Bhagawan Sri Sathya Sai Baba and thank the Sri Sathya Sai Central Trust for providing synthesis and characterization facilities at Central Research Instruments Facility (SSSIHL-CRIF). The authors also thank Japan Advanced Institute of Science and Technology, Japan for providing with XPS characterization facility.

References

1 N. A. Spaldin, *MRS Bull.*, 2017, **42**, 385–389.
2 S. Cao, H. Zhao, B. Kang, J. Zhang and W. Ren, *Sci. Rep.*, 2015, **4**, 5960.
3 S. M. Yusuf, A. Kumar and J. V. Yakhmi, *Appl. Phys. Lett.*, 2009, **95**, 11–14.
4 J. Mao, Y. Sui, X. Zhang, Y. Su, X. Wang, Z. Liu, Y. Wang, R. Zhu, Y. Wang, W. Liu and J. Tang, *Appl. Phys. Lett.*, 2011, **98**, 2009–2012.
5 C. W. Nan, M. I. Bichurin, S. Dong, D. Viehland and G. Srinivasan, *J. Appl. Phys.*, 2008, **103**, 031101.
6 L. Mitoseriu, *Bol. Soc. Esp. Ceram. Vidrio*, 2005, **44**, 177–184.
7 H. Schmid, *J. Phys.: Condens. Matter*, 2008, **20**, 434201.
8 G. King and P. M. Woodward, *J. Mater. Chem.*, 2010, **20**, 5785–5796.
9 N. Singh, J. Y. Rhee and S. Auluck, *J. Korean Phys. Soc.*, 2008, **53**, 806–811.
10 D. Van Tac, V. O. Mittova and I. Y. Mittova, *Inorg. Mater.*, 2011, **47**, 521–526.
11 X. Yuan, Y. Sun and M. Xu, *J. Solid State Chem.*, 2012, **196**, 362–366.
12 P. S. J. Bharadwaj, S. Kundu, K. Vijay Sai and K. B. R. Varma, *J. Phys.: Condens. Matter*, 2020, **32**, 035810.
13 M. Wang and T. Wang, *Materials*, 2019, **12**, 1–11.
14 N. O. Khalifa, H. M. Widatallah, A. M. Gismelseed, F. N. Al-Mabsali, R. G. S. Sofin and M. Pekala, *Hyperfine Interact.*, 2016, **237**, 46.
15 M. C. Carotta, G. Martinelli, Y. Sadaoka, P. Nunziante and E. Traversa, *Sens. Actuators, B*, 2002, **48**, 270–276.
16 J. Ding, X. Lü, H. Shu, J. Xie and H. Zhang, *Mater. Sci. Eng. B Solid State Mater. Adv. Technol.*, 2010, **171**, 31–34.
17 R. L. Zhang, C. Le Chen, K. X. Jin, L. W. Niu, H. Xing and B. C. Luo, *J. Electroceram.*, 2014, **32**, 187–191.
18 M. Siemons, T. Weirich, J. Mayer and U. Simon, *Z. Anorg. Allg. Chem.*, 2004, **630**, 2083–2089.
19 Z. Zhou, L. Guo, H. Yang, Q. Liu and F. Ye, *J. Alloys Compd.*, 2014, **583**, 21–31.
20 R. D. Shannon, *Acta Crystallogr., Sect. A: Cryst. Phys., Diffr., Theor. Gen. Crystallogr.*, 1976, **32**, 751–767.
21 M. O'Keeffe and B. G. Hyde, *Acta Crystallogr., Sect. B: Struct. Crystallogr. Cryst. Chem.*, 1977, **33**, 3802–3813.
22 E. VenkataRamana, F. Figueiras, A. Mahajan, D. M. Tobaldi, B. F. O. Costa, M. P. F. Graca and M. A. Valente, *J. Mater. Chem. C*, 2016, **4**, 1066–1079.
23 A. Shokri, S. Farjami and K. Boustani, *Ceram. Int.*, 2018, **44**, 22092–22101.
24 P. Kubelka, *J. Opt. Soc. Am.*, 1948, **38**, 448–457.
25 V. Gopalan, S. W. Cheong, J. L. Musfeldt, N. High and M. Field, *Phys. Rev. B: Condens. Matter Mater. Phys.*, 2009, **79**, 4–7.

26 J. H. Jung, M. Matsubara, T. Arima, J. P. He, Y. Kaneko and Y. Tokura, *Phys. Rev. Lett.*, 2004, **93**, 1–4.
27 A. S. Moskvin, A. A. Makhnev, L. V. Nomerovannaya, N. N. Loshkareva and A. M. Balbashov, *Phys. Rev. B: Condens. Matter Mater. Phys.*, 2010, **82**, 035106.
28 Y. Tanabe, *J. Phys. Soc. Jpn.*, 1956, **11**, 864–877.
29 T. Matsui, E. Taketani, R. Sato and K. Morii, *J. Phys. D: Appl. Phys.*, 2007, **40**, 6066–6070.
30 M. Asim Farid, H. Zhang, X. Lin, A. Yang, S. Yand, G. Li, F. Liao and J. Lin, *RSC Adv.*, 2015, **5**, 12866–12871.
31 H. Aono, M. Sato, E. Traversa and M. Sakamoto, *J. Am. Ceram. Soc.*, 2001, **47**, 341–347.
32 A. Jaiswal, R. Das, S. Adyanthaya and P. Poddar, *J. Phys. Chem. C*, 2011, **115**, 2954–2960.
33 P. W. Anderson, *Phys. Rev.*, 1959, **115**, 2–13.
34 K. T. Jacob, G. Rajitha and N. Dasgupta, *Indian J. Eng. Mater. Sci.*, 2012, **19**, 47–53.
35 S. Mori, *J. Phys. Soc. Jpn.*, 1970, **28**, 44–50.
36 T. Matsui, H. Tanaka, N. Fujimura, T. Ito, H. Mabuchi and K. Morii, *Appl. Phys. Lett.*, 2002, **81**, 2764–2766.